Measurement of differential cross sections for the deuteron-proton breakup reaction at 160 MeV

W. Parol,[1,*] A. Kozela,[1] K. Bodek,[2] A. Deltuva,[3] M. Eslami-Kalantari,[4] J. Golak,[2] N. Kalantar-Nayestanaki,[5] G. Khatri,[6] St. Kistryn,[2] B. Kłos,[7] J. Kuboś,[1] P. Kulessa,[8] A. Łobejko,[7] A. Magiera,[2] H. Mardanpour,[5] J. G. Messchendorp,[5] I. Mazumdar,[9] R. Skibiński,[2] I. Skwira-Chalot,[10] E. Stephan,[7] A. Ramazani-Moghaddam-Arani,[11] D. Rozpędzik,[2] A. Wilczek,[7] H. Witała,[2] B. Włoch,[1] A. Wrońska,[2] and J. Zejma[2]

[1]*Institute of Nuclear Physics Polish Academy of Sciences, PL-31342 Kraków*
[2]*M. Smoluchowski Institute of Physics, Jagiellonian University, PL-30348 Kraków, Poland*
[3]*Institute of Theoretical Physics and Astronomy, Vilnius University, Vilnius, Lithuania*
[4]*Department of Physics, School of Science, Yazd University, Yazd, Iran*
[5]*KVI-CART, University of Groningen, NL-9747 AA Groningen, The Netherlands*
[6]*CERN, CH-1211 Geneva 23, Switzerland*
[7]*Institute of Physics, University of Silesia, PL-41500 Chorzów, Poland*
[8]*Forschungszentrum Juelich IKP, DE-52425 Juelich, Germany*
[9]*Tata Institute of Fundamental Research, Mumbai 400 005, India*
[10]*Faculty of Physics, University of Warsaw, PL-02093 Warsaw, Poland*
[11]*Departments of Physics, Faculty of Science, University of Kashan, Kashan, Iran*

(Received 7 April 2020; accepted 23 October 2020; published 20 November 2020)

Differential cross sections for the deuteron breakup ^{1}H$(d, pp)n$ reaction were measured for a large set of 243 geometrical configurations at the beam energy of 80 MeV/nucleon. The cross-section data are normalized by the luminosity factor obtained on the basis of a simultaneous measurement of the elastic-scattering channel and the existing cross-section data for this process. The results are compared with the theoretical calculations modeling nuclear interactions with and without taking into account the three-nucleon force (3NF) and the Coulomb interaction. In the validated region of the phase space, both the Coulomb force and 3NF play an important role in providing a good description of the data. There are also regions in which description improvements due to the inclusion of 3NF are insufficient.

DOI: 10.1103/PhysRevC.102.054002

I. INTRODUCTION

One of the most basic topics in modern nuclear physics is the nature of the forces acting between nucleons. Exact knowledge of all the features of two-nucleon (NN) system dynamics should provide a basis for understanding the properties and interactions in heavier systems. This presumption has been verified by the application of models of the NN interaction to describe systems composed of three nucleons (3N). Theoretical predictions of observables are obtained by means of a rigorous solution of Faddeev equations [1–4], including the NN interaction as the so-called realistic potential models, based on the meson exchange theory, originally proposed by Yukawa [5] and confirmed by Occhialini and Powell [6]. Early stages of experimental studies of the deuteron-proton elastic scattering in the range of intermediate energies and theoretical efforts [7] have proven the dominant, but not sufficient, role of the pairwise NN interaction. The missing piece of dynamics, referred to as the three-nucleon force (3NF), also has an impact. The effects of this force, significantly smaller than the pairwise NN contribution, are visible in systems consisting of at least three nucleons. Modern NN potentials like Argonne V18 (AV18) [8], CD Bonn (CDB) [9], and Nijmegen I and II [10] have yielded a remarkably good agreement (with a χ^2/d.o.f. of approximately 1) between the predictions of calculations with experimental data for the two-nucleon systems. To describe three-nucleon systems, realistic NN potentials are used in Faddeev equations together with the present models of 3NF like Urbana IX [11] or Tucson-Melbourne [12]. In another approach, the three-nucleon interaction can be introduced within the coupled-channel (CC) framework by an explicit treatment of the Δ-isobar excitation [13–15]. Alternatively, contributions of NN and 3NF to the potential energy of a 3N system can be calculated within the chiral effective-field theory (ChEFT) [16,17]. Here, the many-body interactions appear naturally at higher orders (nonvanishing 3NF at next-to-next-to leading order). Modern calculations also include other ingredients of few-nucleon dynamics, such as the Coulomb interactions [18,19] or relativistic effects [20,21]. The predicted effects in differential cross sections emerge

*wiktor.parol@ifj.edu.pl; wiktor.parol@gmail.com

in various parts of the phase space of the deuteron-proton breakup reaction with different magnitude. The existing experimental data [22–28] demonstrate quite sizable 3NF and Coulomb effects and confirm their importance for the correct description of differential cross sections for the deuteron breakup reaction at energies above 65 MeV/nucleon and below 200 MeV/nucleon.

ChEFT is still under development, and consistent calculations at N3LO required for precise studies of the elastic scattering and breakup reaction at intermediate energies are necessary. Recently, with the development of calculation methods for many-nucleon systems, the ChEFT potentials have been used for calculations of ground and low-lying excited states of light and medium-mass nuclei, and of nuclear radii. The 3NF turned out to be crucial for a correct description of the shell structure of neutron-rich nuclei and the nature of nuclear matter [29–31]. The nucleon-deuteron scattering observables serve as a very important test ground for verifying such potentials. Additionally, they are considered as constraints for fixing the so-called low-energy constants, c_D and c_E, entering the 3NF constructed within the ChEFT approach [32]. This, in turn, is highly significant from the perspective of a consistent description of nuclei and nuclear matter [33].

The present work is a continuation of an experimental campaign focusing on studying contributions from various dynamical components (3NF, Coulomb force, and relativistic component) of nuclear interactions by measuring various observables in few-nucleon systems for large parts of the phase space. The measured differential cross sections at 80 MeV/nucleon enlarge the systematic database for the deuteron-proton breakup reaction at intermediate energies. The generated feedback allows for further validation of the available and future theoretical models of nuclear interaction.

In Sec. II, the experimental setup is described. Section III provides an overview of the analysis of data, and Sec. IV presents the results obtained. Section V summarizes the main outcome of the presented studies.

II. EXPERIMENT

The experiment was performed at the Kernfysisch Versneller Instituut (KVI) in Groningen, the Netherlands (currently KVI-CART). The deuteron breakup reaction, $^1H(d, pp)n$, was measured simultaneously with the elastic scattering of deuterons in a liquid hydrogen target. A deuteron beam of 80 MeV/nucleon energy was provided by the Accelerateur Groningen-Orsay (AGOR) cyclotron [34], and the charged products of reaction were detected by the Big Instrument for Nuclear-polarization Analysis (BINA) [35] system. The BINA detection system was characterized by high angular acceptance (nearly 4π), good (in the forward region) and moderate (in the backward part) angular resolution, and the ability to identify and provide complete kinematical information for two or more charged particles in the final state. All these features made the BINA detector an excellent tool for studying the few-nucleon systems in the intermediate energy range.

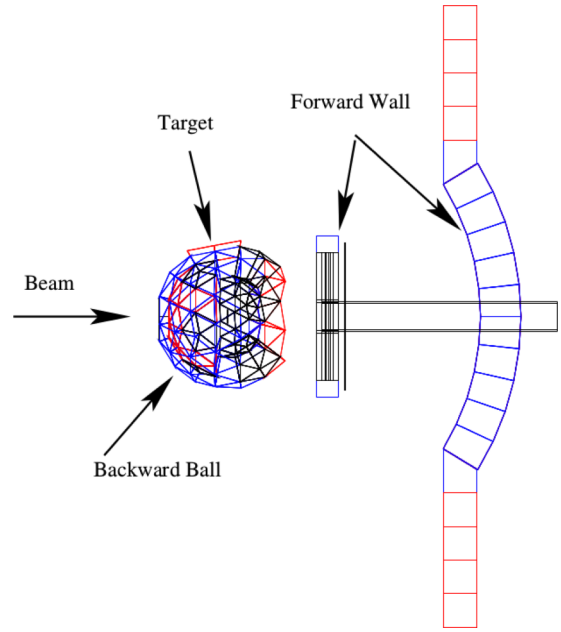

FIG. 1. Schematic side view of the BINA detection system.

The BINA detection system, Fig. 1, is comprised of two main parts, the forward Wall and the backward Ball. The liquid hydrogen target cell was positioned in the center of the Ball, which in this experiment served only as the scattering chamber. The front part, the Wall, consisted of three detector elements positioned in planes perpendicular to the beam line: a multiwire proportional chamber (MWPC) and two scintillator hodoscopes, forming a set of 120 ΔE-E virtual telescopes. The Wall was optimized for detecting protons and deuterons in the energy ranges of 20–130 MeV and 25–200 MeV, respectively.

Precise measurement of scattering angles was accomplished by MWPC [36] positioned directly behind the thin vacuum window, as the first detector was intersected by the reaction products. It consisted of three active planes: the plane measuring the x coordinate with vertical wires, the plane measuring the y coordinate with horizontal wires, and the diagonal plane U with wires inclined by 45 degrees. All wires within a plane were 2 mm apart and were combined in pairs to form the 118, 118, and 148 separate detector channels for the X, Y and U planes, respectively. The active area of the MWPC was 38×38 cm^2. It formed a pixel system allowing for precise determination of the crossing point of a charged particle, and, thus, for the reconstruction of the emission angles of the outgoing reaction products. The angular acceptance of the detector in polar angles was $\vartheta \in (10^\circ, 40^\circ)$, with the full azimuthal coverage up to 30°.

The ΔE transmission detector comprised of 24 vertical strips of a 2-mm-thick plastic scintillator (BICRON type BC-408 [37]). The signals from each ΔE stripe were read by one photomultiplier tube (PMT) coupled with a light guide modeled for optimal light collection. As the signals were proportional to the specific energy loss of charged particles, they played an essential role in particle identification.

The E detector was made of horizontally arranged 120-mm-thick scintillator slabs (BICRON type BC-408 [37]). To minimize particle crossovers between neighboring scintillators, the ten central elements of the E detector followed a cylindrical symmetry, with the cylinder center at the target position (see Fig. 1). The ten additional elements attached to the top and bottom of the cylindrical part were not used in the present experiment. The energy deposited by particles in the E slab was converted to scintillation light registered by two PMTs attached to both ends of each detector. This allowed for compensation for the light attenuation along the scintillator resulting in a position-independent output.

Other details concerning the setup as well as the electronic and read-out systems used in the experiment can be found in Ref. [38]. The data-acquisition system was based on GSI Multi-Branch System (MBS) [39].

III. DATA ANALYSIS

Data analysis started with the selection of time periods characterized by a stable operation of the cyclotron and all elements of the detector. The selection was based on the scaler rates recorded for all individual channels of the detector. To minimize random coincidences, additional time gates rejecting particles not correlated with the trigger signal had been set.

A. Reconstruction of particle momentum

1. Track reconstruction

Charged particles passing through the Wall detector deposit their energy successively in the MWPC, ΔE and E. In the simplest case, for a single particle, only three wires (one wire per plane) in the MWPC give a signal, while in reality clusters of two or more wires are observed. When no signal amplitude from the MWPC was collected, the hit position was represented by the center of the cluster.

Particle angles were reconstructed, assuming that they were emitted from the target center, and using the position information from the MWPC. Additionally, correct matching with hits in the ΔE and E scintillators was required. Cuts on the matching were wide enough to accept all the tracks of particles not scattered on their way from the target to the E detector. As a result, the track reconstruction efficiency could be reduced to the product of independent detection efficiencies, as discussed in Sec. III C. There are several strategies of track-position reconstruction on the basis of the information from the three MWPC planes. In the analysis published in several earlier papers, e.g., in Ref. [40], a coincidence of all three planes was required, with the X and Y planes defining the (x, y) coordinates of the intersection of the track with the MWPC, and the U plane used to validate this intersection. In the data analysis of deuteron-deuteron scattering presented in Ref. [41], we also accepted events with only two planes hit, provided that no other hits were present in the MWPC, and the resulting position information was correlated with hits in the ΔE and E detectors. This kind of tracks, hereinafter referred to as the "weak tracks" (as opposed to "full tracks" indicating three-plane coincidences), is important for the consideration of systematic effects, such as energy- and position-dependent

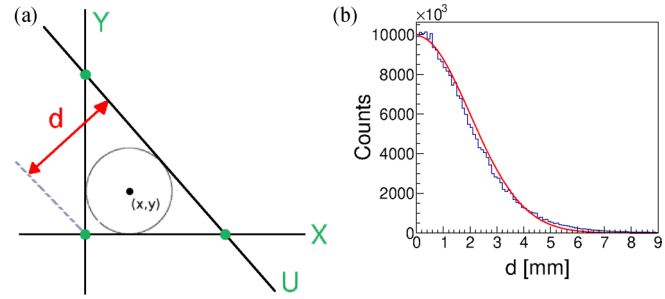

FIG. 2. (a) Geometrical reconstruction of the (x, y) coordinates of the full-track intersection with the Y plane. Lines X, Y, and U represent centroids of clusters in the respective planes projected onto the Y plane. Reconstructed (x, y) coordinates for all three types of weak tracks are shown as green dots. (b) Distribution of d [defined in panel (a)] for the whole dataset. Limit of 7 mm for d corresponds to the $\approx 3\sigma$ of the fitted Gaussian distribution (red solid line).

MWPC efficiency. The analysis presented in this paper was based on full-tracks and, additionally, we took advantage of the position information provided by the U plane. In this case, the final position was given by the center of a circle inscribed in the triangle defined by the corresponding cluster centroids projected (from the target center direction) onto a common plane (see Fig. 2). Assuming equal position resolution of all planes, this algorithm improves the final angular resolution for the polar angle ϑ up to 0.4° and the azimuthal angle φ to 0.67°–1.39° (depending on the polar angle). It is also clear that the weak tracks involving the U plane feature lower position resolution in one direction than those defined by the X and Y planes. It is worth noting that three-dimensional track parameters, in this case the polar and azimuthal angles, can be obtained by using the following formulas:

$$\vartheta = \arctan\left(\frac{\sqrt{x^2 + y^2}}{Z_Y}\right), \tag{1}$$

$$\varphi = \text{atan2}(y, x), \tag{2}$$

under the assumption that the corresponding particle was emitted from the target center (Z_Y is the distance of the projection plane from this center). The atan2() function calculates the principal value of the $\arctan(\frac{y}{x})$, using the signs of the two arguments to determine the quadrant of the result [42]. Smearing of the reaction point due to target thickness and beam size was included in the systematic uncertainty of the final results. Having these parameters, it was possible to check if the track coincided, within the given position resolution, with hits in the E and ΔE detector elements—only these events were considered in further analysis. To combine the hits in individual planes into a full-track event, a cut was imposed on the distance between the centroid of the cluster reconstructed in the U plane and the cross-point between centroids in the X and Y planes (variable d in Fig. 2).

2. Particle identification

Neglecting traces of heavier ions from beam interactions with the target frames, the particle identification could be reduced in this experiment to the simple distinction between

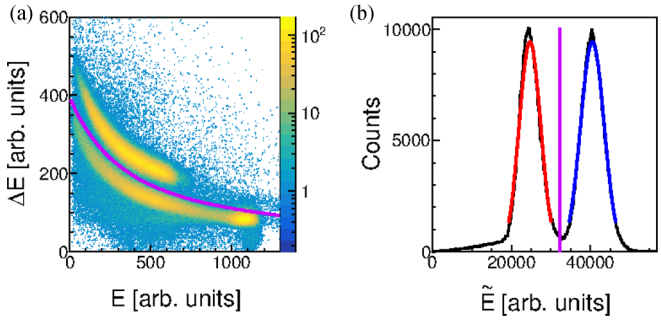

FIG. 3. Example of the identification spectra for a selected virtual telescope ($\Delta E = 13$, $E = 8$). (a) ΔE-E signal distribution. The violet line separates the proton and deuteron bands and corresponds to the vertical line indicated in the distribution on the right side. (b) Projection of the linearized spectrum onto the $\widetilde{E}$ variable. The two peaks correspond to the proton and deuteron bands. The 2σ ranges of the fitted Gaussian functions are shown as red and blue lines for protons and deuterons, respectively.

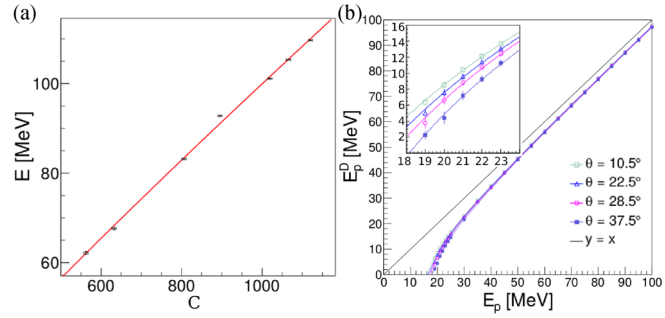

FIG. 4. Energy calibration. (a) Example of the correlation between experimentally obtained centroids of the distribution of the C variable and of the corresponding distribution of the simulated energy deposited in the E detector together with the fitted function defined in Eq. (3). (b) Set of polynomials transforming the energy deposited by proton, $E^D(\vartheta)$, to its initial kinetic energy at the reaction point.

protons and deuterons, where the latter came exclusively from the elastic scattering. The identification was based on the linearization technique applied to the ΔE-E spectra [43]. It allowed for the identification of reaction products by analytically determined conditions. Following the simplified consideration based on the Bethe-Bloch formula, a new variable $\widetilde{E} = (E + \Delta E)^{\kappa} - E^{\kappa}$ was introduced, the value of which was constant for all particle types in a wide energy range [44]. The κ index characterized the detector material, its internal structure (variations of transparency, quality of the surface) and geometry and was determined for each virtual telescope separately.

As a result, a one-dimensional distribution of the $\widetilde{E}$ variable was obtained in which protons and deuterons were visible as distinct peaks (Fig. 3). To improve the sensitivity of this method, the fine tuning of κ (as well as of the μ_p, σ_p, μ_d, σ_d parameters corresponding to the centroids and widths of the proton and deuteron peaks, respectively) was performed for each virtual ΔE-E telescope. For this purpose, a sample of the data with a well-balanced number of protons and deuterons (from dd scattering experiment at the same beam energy) was used. The κ index has been varied to get a maximum separation between the proton and deuteron peaks. The obtained final values of κ ranged from 1.63 to 1.85, while according to the Bethe-Bloch rule, $\kappa = 1.73$ was expected for an ideal scintillator. This method allowed for controllable selection of different event samples not biased by subjective cuts.

3. *Energy reconstruction*

Energy calibration provides a relationship between the recorded ADC channel and the deposited energy E^D in a given scintillator element. Since 2-mm-thick ΔE stripes decrease particle energy by a relatively small fraction, and this information is strongly biased by light attenuation along the scintillator and the light guide, only an E detector was used for the reconstruction of particle energies. The calibration was carried out using protons from elastic scattering and the Monte Carlo simulations, including full detector geometry implemented in the GEANT4 simulation package [45,46]. The detector was characterized by a noticeable variation of the PMT signal amplitude, depending on the point of interaction along the scintillator. This dependence, caused by light attenuation and losses, can be significantly suppressed by applying the geometrical mean of responses of the left and right PMTs ($C = \sqrt{c_L c_R}$). For the two middle E slabs partially cut in the center in order to accommodate an opening for the beam pipe, a plain sum of the signals ($C = c_L + c_R$) was applied. The remaining small dependence of the signal on position was taken into account in the position-dependent energy calibration.

To extend the calibration over energies of protons from the breakup reaction, a dedicated measurement was performed by using energy degraders placed between the ΔE and E detectors. The degraders were made of steel plates of precisely defined thickness values, which were mounted in several configurations, allowing for a satisfactory coverage of the energy range. The elastically scattered protons were selected according to the kinematic conditions: coplanarity and ϑ_p vs ϑ_d relationships. The detector plane was divided into 180 sectors, each labeled by the side ($s =$ left, right), E-scintillator element number ($N = 0, 1, \ldots, 9$), and the polar angle bin number ($\bar{\vartheta} = 0, \ldots, 8$). All of the sectors were calibrated separately using the information from the GEANT4 simulations and the following two-parameter function:

$$E^D_{s,N,\bar{\vartheta}}(C) = a_{s,N,\bar{\vartheta}} C + b_{s,N,\bar{\vartheta}} \sqrt{C}, \tag{3}$$

where $E^D_{s,N,\bar{\vartheta}}(C)$ stands for the energy deposited in this particular detector element as a function of variable C, i.e., the combination of signals from the left and right PMTs defined above. An example of the fit is shown in Fig. 4(a).

Deuteron energy calibration was based on the one performed for protons and corrected for a different light output corresponding to the same energy deposited by particles of a different mass. The particle-dependent light output for the known scintillator material was taken from Bicron data sheets [37], and additionally validated in dedicated studies (see Ref. [47] for details).

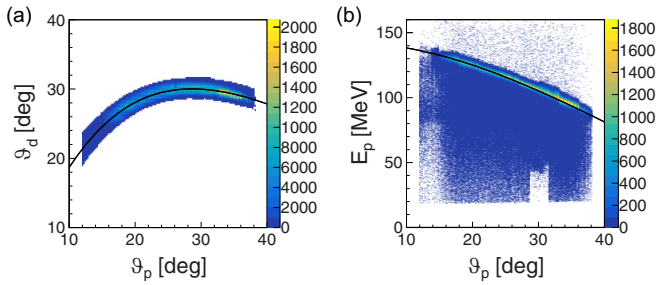

FIG. 5. (a) Kinematic relation between the polar angles of coincident coplanar particles with $\pm 3\sigma$ cut around the theoretical kinematics of dp elastic scattering (black line). (b) Energy distribution of particles identified on the basis of coplanarity and polar angle cut (shown in the left panel) as elastically scattered protons.

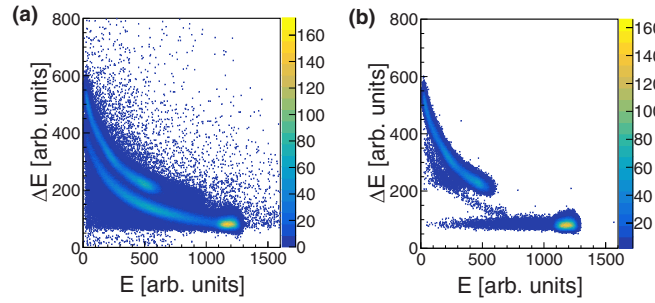

FIG. 6. Relation of particle energies deposited in the chosen ΔE-E telescope ($E = 1$, $\Delta E = 9$). (a) Spectrum for particles registered in coincidence with any other particle in the Wall. (b) The same with the additional condition that coincident particles meet angular kinematical relations of elastic scattering.

To reproduce the initial kinetic energy of a particle at the reaction point (E_i), a conversion formula was developed based on the energy loss of simulated monoenergetic protons and deuterons on their way to and inside the E detector:

$$E_i(\vartheta) = P^8_{i,\vartheta}\left(E_i^D(\vartheta)\right), \tag{4}$$

where subscript i stands for particle type (proton or deuteron) and $\{P^8_{i,\vartheta}\}$ is a set of eighth-order polynomials with factors calculated from the deposited-to-initial energy relations obtained from the GEANT4 simulations of the experiment [see Fig. 4(b)]. The final energy resolution reached 2.1% for 123 MeV protons and deteriorates with energy in accordance with photon statistics.

B. Process identification

Neglecting small admixtures of electromagnetic processes, the deuteron-proton interaction in the investigated energy range may result in elastic scattering or breakup. A deuteron in the exit channel uniquely identifies the reaction as elastic scattering, while two protons must be identified in order to identify the breakup reaction. This goal can be accomplished for most of the recorded events using the PID procedure described in Sec. III A 2. On the other hand, precise measurements of angles and strict kinematic relations of the scattering angles and energies in the elastic deuteron-proton scattering (Fig. 5) allow for correct identification of the process, even when the regular PID method fails. As a result, two-track events can be identified as deuteron-proton elastic scattering even if one or both particles undergo hadronic interaction in the thick scintillator, which influences the energy measurement and prevents successful application of the ΔE-E-based PID method (Fig. 6).

C. Detector efficiency

Determination of a true number of events of a given type from the number of events registered by the detector required knowledge of the detector efficiency. Since successful registration of a single particle is contingent upon complete information from three detectors (MWPC, ΔE, and E), the total detection efficiency $\varepsilon(x, y)$ could be considered a product of individual efficiencies of those detectors:

$$\varepsilon(x, y) = \varepsilon_{\mathrm{MWPC}}(x, y)\varepsilon_{\Delta E}(x, y)\varepsilon_E. \tag{5}$$

The efficiency of the E detector (ε_E) was assumed to be 100%. This was justified by a very tight fitting of the detector slabs. The gap between the adjacent elements is of the order of 50 microns compared with 10-cm width of the front face of each element. Therefore, the problem of efficiency was reduced to the particle-type-dependent energy threshold.

Since the main sources of inefficiency for both the ΔE and MWPC detectors were well localized, the construction of position-dependent efficiency maps was required to properly account for them. This was made possible by the use of position information from MWPC.

The efficiency of the ΔE detector, $\varepsilon_{\Delta E}(x, y)$ [Fig. 7(d)] was calculated directly on the basis of single-particle events

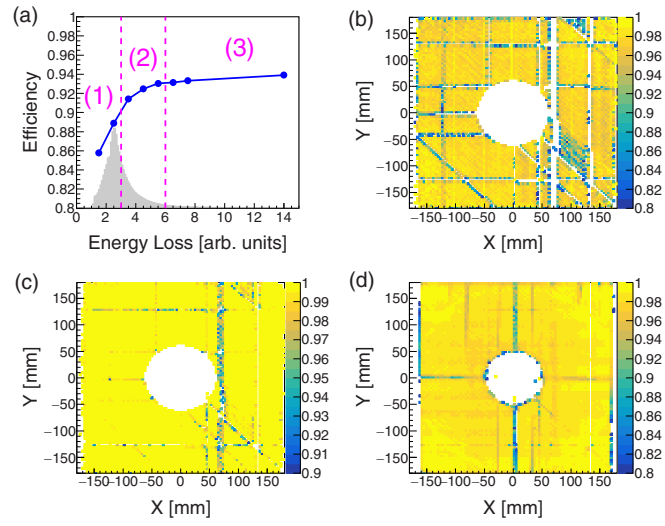

FIG. 7. (a) The average MWPC efficiency (blue dots connected by a line) as a function of energy loss in a gas mixture, Eq. (9). The distribution of events is shown in gray. (b), (c) Position dependence of the MWPC efficiency shown only for the range (1), separately for (b) full and (c) weak tracks. (d) Analogous map of the ΔE efficiency.

according to the following formula:

$$\varepsilon_{\Delta E}(x, y) = \frac{N_{\mathrm{ref}+\Delta E}(x, y)}{N_{\mathrm{ref}}(x, y)}, \tag{6}$$

where the reference number of events, N_{ref}, corresponds to the number of all particles registered by MWPC with a correlated hit in the E scintillator, regardless of the ΔE information, while for $N_{\mathrm{ref}+\Delta E}$, additional matching with information from the ΔE detector was required.

Position-dependent efficiency maps of the multiwire proportional chamber were obtained from single-plane efficiencies ($\varepsilon_X, \varepsilon_Y, \varepsilon_U$) according to the following formulas:

$$\varepsilon_{\mathrm{MWPC}}(x, y) = \varepsilon_X(x, y)\varepsilon_Y(x, y)\varepsilon_U(x, y), \tag{7}$$

$$\begin{aligned}\varepsilon^{\mathrm{weak}}_{\mathrm{MWPC}}(x, y) = {} & \varepsilon_{\mathrm{MWPC}}(x, y) \\ & + \varepsilon_X(x, y)\varepsilon_Y(x, y)[1 - \varepsilon_U(x, y)] \\ & + \varepsilon_X(x, y)[1 - \varepsilon_Y(x, y)]\varepsilon_U(x, y) \\ & + [1 - \varepsilon_X(x, y)]\varepsilon_Y(x, y)\varepsilon_U(x, y).\end{aligned} \tag{8}$$

The first one [Eq. (7)] corresponds to full tracks, when the coincidence of all three planes was required, and the second one [Eq. (8)]—to the analysis, in which weak tracks were also accepted (see Sec. III A 1). Efficiencies of individual planes were calculated by using position information from the remaining two planes, and requiring information from both scintillator hodoscopes, in a way analogous to the one already introduced for ΔE. It is clear that the efficiency in the approach allowing for weak tracks was significantly less sensitive to local defects (dead channels) present in each plane. The average efficiency in this case was as high as 98% [see Fig. 7(c)], compared with 85% for full tracks [see Fig. 7(b)]. To better understand the systematics associated with the MWPC efficiency, a full analysis of cross sections was performed with and without accepting weak tracks. The good agreement obtained strengthens our confidence in the final results of efficiency calculations [48]. The data analysis is based on full tracks, due to better angular resolution achieved in this manner.

The MWPC efficiency also depends on the particle type and energy, and this effect is visible in efficiency maps for full tracks. This, in fact, can be traced back to the dependence on the relative energy loss of a given particle within the detector gas mixture. To account for this effect, a new variable was introduced:

$$E_{\mathrm{loss}} \sim q^2 \frac{m}{E_k}, \tag{9}$$

where q and m are the particle charge and mass, while E_k denotes their kinetic energy. This variable was normalized by assigning the value 1 to the most energetic of all the recorded particles, elastically scattered protons. Figure 7(a) presents the distribution of E_{loss} (regardless of the particle type) and the average efficiency obtained for various bins in E_{loss}. In the final analysis, in order to maintain acceptable statistics in each bin of the efficiency map, only three satisfactorily populated ranges of E_{loss} were defined, as shown in Fig. 7(a). The final efficiency map for minimum ionizing particles [Fig. 7(b)] recorded in this experiment [region marked as (1) in E_{loss} distribution] was compared with the efficiency maps constructed for $\varepsilon^{\mathrm{weak}}_{\mathrm{MWPC}}$ [Fig. 7(c)]. Due to contact problems at hardly accessible places, certain electronic channels of the MWPC were not working. There are many inefficient regions in the MWPC, especially for full tracks corresponding to region (1) of E_{loss}. The correction defined in Eq. (7) was not effective for crossing inefficient wires in two or more planes. In any such cases or in more general cases of low final detector efficiency $\varepsilon(x, y) < 0.5$ [Eq. (5)], the affected detector region was rejected from the analysis. The acceptance loss was calculated with the Monte Carlo simulation and corrected, as described in the next section.

1. Configurational efficiency

When two particles enter the same detector element, the reconstructed information gets distorted. This leads to a false energy reconstruction and may interfere with particle identification. This effect, hereinafter referred to as the configurational efficiency, strongly depends on the geometry of the final state and of the detector and can be accounted for by the Monte Carlo simulations.

Due to the coplanarity condition, the loss of events corresponding to the elastic scattering caused by configurational efficiency was practically negligible. For the breakup reaction the efficiency strongly depends on breakup kinematics, defined by polar angles of emission of both the protons, ϑ_1 and ϑ_2, and the relative azimuthal angle, φ_{12}, between them. Due to the axial symmetry of the cross section, the thus-defined configuration was rotated around the beam axis. The configurational efficiency was determined by the analysis of a set of breakup events simulated with the use of the GEANT4 framework with the Wall detector geometry included. Since good statistical accuracy of this correction has been ensured, the only significant uncertainty may originate from the inaccuracies of the experimental setup (detector or beam geometry) and the applied model of the event generator. Subsequently, a uniform three-body breakup phase-space distribution was used, which was well justified in the case of narrow angular ranges applied when defining the configuration. The configurational efficiency for a given geometry $(\vartheta_1, \vartheta_2, \varphi_{12})$ was defined as the ratio of the number of events for which both particles were registered by separate detector elements, to the number of all simulated events. As expected, the configuration efficiency grew with the increase of φ_{12}, with pronounced local minima reflecting the structure of the E detector (Fig. 8). Due to the much finer granularity of the MWPC compared with hodoscopes, the contribution of this detector to the configurational efficiency was very small. In the simulation, the distribution of cluster sizes observed in the experiment was used to account for hit losses resulting from the coalescence of clusters produced by different particles. The final correction for acceptance losses took into account the losses resulting from two particles registered in the same element and the earlier-discussed regions of low efficiency. It is calculated as follows:

$$\varepsilon_c(\xi) = \frac{N_{\mathrm{rec}}(\xi)}{N_{\mathrm{tot}}(\xi)}, \tag{10}$$

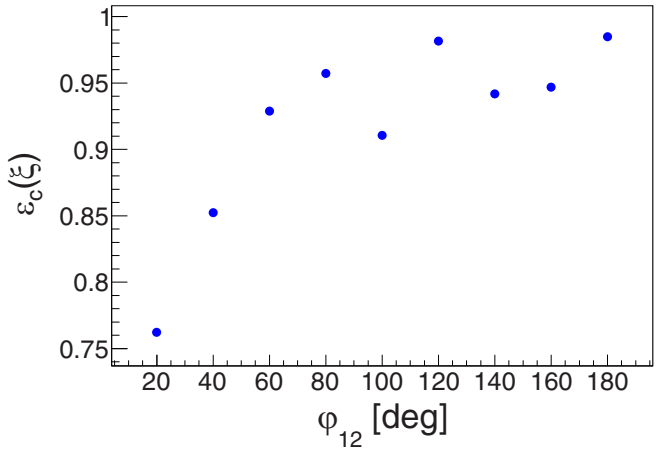

FIG. 8. Configurational efficiency for a set of breakup proton-proton configurations characterized by $\vartheta_1 = 27^\circ$, $\vartheta_2 = 21^\circ$, and $\Delta\varphi = 10^\circ$. The general trend, also observed for other combinations of polar angles, shows the decrease of efficiency with dropping relative azimuthal angle between protons, φ_{12}, with the local minima determined by the geometry of the E detector.

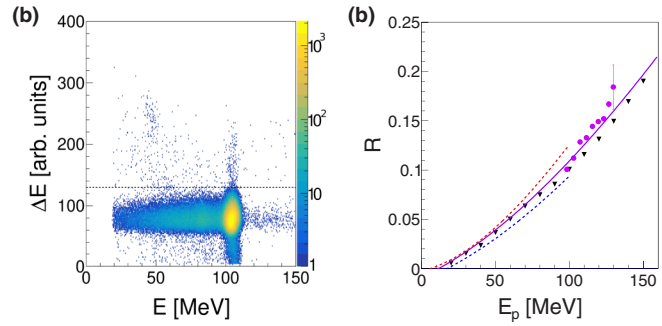

FIG. 9. (a) Sample of ΔE-E spectrum for the selected polar angle of elastically scattered protons $\vartheta_p = 31^\circ \pm 1^\circ$. Horizontal band extending on the left from elastic spot corresponds to the hadronic interactions decreasing the registered energy. The events below the dashed line are used in the calculation of the tail-to-peak ratio R. (b) Obtained tail-to-peak ratio (points) compared with the theoretical calculations at lower energies [49] (lines) and to simulations [40] (triangles). Solid line represents predictions of a simple model based on the material composition of the scintillator [49] extrapolated to energies over 100 MeV.

where ξ defines the geometry of the reaction products: $\xi = \{\vartheta_1, \vartheta_2, \varphi_{12}\}$ for the breakup reaction and $\xi = \{\vartheta_p\}$ for the elastic-scattering channel, N_{tot} is the total number of coincidences generated for this configuration, and N_{rec} counts only the events successfully recorded by the virtual BINA detector. The total correction factor related to the efficiencies for registering the number N of coincident events in the selected configuration ξ can be noted as

$$\varepsilon_N^{\xi} = N\varepsilon_c(\xi)\left(\sum_{\langle i,j\rangle}\frac{1}{\varepsilon(x_i,y_i)\varepsilon(x_j,y_j)}\right)^{-1}, \tag{11}$$

where $\varepsilon(x_i, y_i)$ is the single-particle efficiency defined in Eq. (11) and $\langle i, j\rangle$ symbolizes the set of N coincident pairs.

2. *Hadronic reactions*

The calibration and particle identification procedures fail when the particle undergoes a hadronic reaction with large momentum transfer on its way to or inside the E detector. In such cases, a part of the particle energy was lost, less light is produced in the scintillator, and, as a result, the reconstructed kinetic energy was underestimated, leading to event rejection due to the PID cut. The amount of the affected events was estimated based on experimental ΔE-E spectra gated by kinematic conditions defining the dp elastic scattering [Fig. 9(a)] in order to reject the breakup band. In these spectra, hadronic interactions are visible as a horizontal band protruding on the low-energy side from the elastic-scattering spot. The number of events integrated within this band was normalized to the number of events inside the elastic peak (tail-to-peak ratio R). The results obtained for several energies are in satisfactory agreement with the theoretical predictions based on the effective inelastic cross-section model for protons in the combination of materials the plastic scintillator is composed [49] extrapolated to energies over 100 MeV [Fig. 9(b)]. Therefore, the R values corresponding to the solid line in Fig. 9, considered as validated, were used in further analysis with up to 3.8% systematic uncertainty. To account for the loss of breakup-originated protons due to hadronic interactions, a dedicated correction factor $\eta(E_p)$ was introduced on the basis of R:

$$\eta(E_p) = 1 + R. \tag{12}$$

In the case of elastic scattering, protons and deuterons were identified on the basis of kinematic angle relationships. As a result, events were lost only if hadronic interactions had occurred before the particle reached scintillators and the corresponding correction was negligible.

D. Luminosity

Direct measurement of absolute differential cross sections requires precise knowledge of the beam current, target thickness and scattering angles of the reaction products. In the present experiment, neither the target cell surface density nor the very low beam current (in the range of a few pA) were known with sufficient precision. The normalization factor had to be obtained on the basis of the simultaneously measured elastic dp scattering and the corresponding cross section derived from previous experiments. Since no published cross-section data for the dp elastic-scattering process at 80 MeV/nucleon exist, a model-independent interpolation was performed based on all the existing experimental data in the range of 65–190 MeV/nucleon [50–53]. The obtained absolute values of the differential cross section, σ_{lab}, agree very well with the theoretical calculations based on the charge-dependent Bonn potential supplemented with the TM99 three-nucleon force [54] (Fig. 10). The reference data were subsequently used to calculate the experimental integrated luminosity according to the formula

$$L(\vartheta_p) = \frac{N_{\text{pd}}(\vartheta_p)}{\sigma_{\text{lab}}(\vartheta_p)\Delta\Omega\varepsilon(\vartheta_p)}, \tag{13}$$

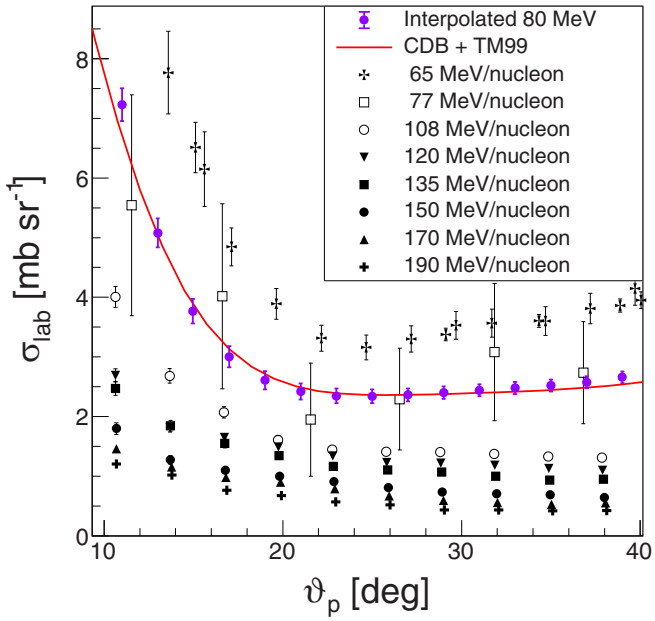

FIG. 10. Interpolated cross section for deuteron-proton elastic scattering at the energy of 80 MeV/nucleon (purple) in the laboratory frame in comparison with the theoretical calculations based on the CDB + TM99 potential [54]. The experimental data used for this interpolation are shown in black.

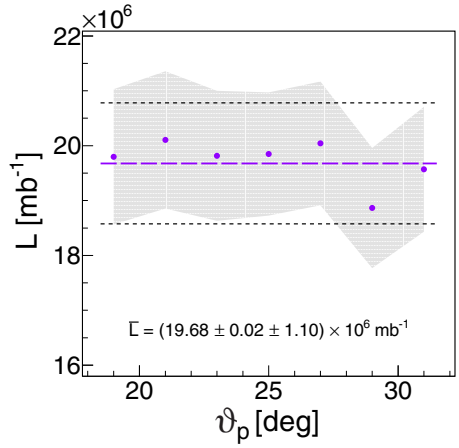

FIG. 11. Luminosity integrated over time determined on the basis of elastic scattering, independently for each proton polar angle. Statistical errors are negligible, while the gray shade corresponds to the range of systematic errors of individual data points. The average value of the luminosity (purple dashed line) is known with the accuracy dominated by systematic uncertainty (dashed black lines).

where $\Delta\Omega$ is the solid angle and $N_{\rm pd}(\vartheta_p)$ is the number of elastically scattered protons recorded in a certain bin in the polar angle of proton emission. To reduce the influence of acceptance losses resulting from reaching the edges of a square-like detector, the elastically scattered particles were collected from a limited space close to the diagonals of the MWPC defined by the azimuthal angle $\varphi_{12} = \{45^\circ, 135^\circ, -45^\circ, -135^\circ\}$ with $\pm 15^\circ$ tolerance.

The values obtained were, as expected, consistent with one another within the experimental uncertainties (Fig. 11). As the final integrated luminosity value, the average $\bar{L} = (19.68 \pm 0.02^{\rm stat} \pm 1 \times 10^{\rm syst}) \times 10^6$ [mb^{-1}] was accepted.

E. Differential cross sections for breakup process

The breakup cross section was determined for 243 angular configurations. The angular range for the integration of events was selected to be 2° in polar and 20° in azimuthal angles. For each configuration, breakup events are placed on the (E_1, E_2) plane, in which they group along the corresponding kinematic curve [Fig. 12(a)]. The width of the distribution in the direction perpendicular to the curve, the D coordinate, depends on energy resolution and the spread of kinematics corresponding to the size of the angular bin. The arc-length measured along the kinematic curve is used to define the S coordinate [55].

The fivefold differential cross section for the deuteron breakup reaction was calculated according to the following formula

$$\frac{d^5\sigma(\xi, S)}{d\Omega_1 d\Omega_2 dS} = \frac{N^{\rm BR}(\xi, S)\eta(E_1)\eta(E_2)}{\varepsilon^{\xi}_{N^{\rm BR}} L \Delta\Omega_1 \Delta\Omega_2 \Delta S}, \qquad (14)$$

where L is the luminosity integrated over time and $N^{\rm BR}$ corresponds to the number of events falling into the chosen geometry ξ within the ranges of integration defined below. ε^{ξ} is the total detector efficiency, as defined in Eq. (11), and $\eta(E_1)$, $\eta(E_2)$ account for the energy-dependent hadronic interaction corrections. The ordering of protons in the case of analysis of symmetric configurations ($\vartheta_1 = \vartheta_2$) was random, while in the case of asymmetric configurations ($\vartheta_1 \neq \vartheta_2$), the proton scattered at a larger polar angle was marked as the first one ($\vartheta_1 > \vartheta_2$).

Determining the cross section started with the measured number of events ($N^{\rm BR}$) from the deuteron breakup channel. All of the accepted events were classified into kinematic configurations defined by scattering angles ($\vartheta_1, \vartheta_2, \varphi_{12}$). The adopted grid assumed nine intervals in the relative azimuthal angle (with the width of $\Delta\varphi_{12} = 20^\circ$) and 27 combinations of intervals in ϑ_1 and ϑ_2 angles, 2° wide. The centers of these

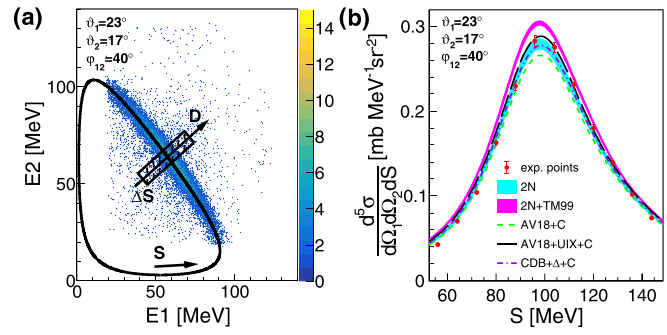

FIG. 12. (a) Distribution of events for a selected breakup configuration together with the corresponding kinematic curve; definitions of the S and D variables are presented graphically. (b) Measured cross-section distribution as a function of the S variable compared with the theoretical predictions for this configuration. See Sec. IV for details of the theoretical models specified in the legend.

TABLE I. Evaluation of total systematic errors.

Normalization factor (luminosity):	
Reconstruction of angles	0.24%
Particle identification	0.7%
Cross section interpolation	4.1%
Breakup cross section:	
Reconstruction of angles	0.15%–0.24%
Particle identification	0.12%–7.6%
Hadronic reactions	3.8%
Configurational efficiency	0.1%–16.3%

intervals were provided by the formula

$$\vartheta_{1,2} = 17^\circ + 2^\circ k, \quad k = 0, 1, 2, \ldots, 6,$$
$$\varphi_{1,2} = 20^\circ j, \quad j = 1, 2, \ldots, 9. \tag{15}$$

For each geometry, the two-dimensional E_2 vs E_1 distribution was constructed and events falling within a single bin in S with $\Delta S = 8$ MeV (see, e.g., a hatched rectangle in Fig. 12) were projected onto the axis locally perpendicular to the S curve (the D coordinate). For each S bin, a Gaussian function was fit to the distribution of events along D and integrated over $\pm 3\sigma$. The resulting N^{BR} value was normalized according to Eq. (14) and the cross-section distribution as a function of S was obtained (see Fig. 12).

F. Experimental uncertainties

The elastic scattering and breakup reactions were measured simultaneously by the same detector and under the same experimental conditions, such as beam current, triggers, dead time, etc. Although some of the systematic effects were the same, the clear differences between both processes (coplanarity of the elastic-scattering kinematics and different particle types in the exit channels) led to a different balance of systematic uncertainties, which is discussed separately for each reaction channel.

For the elastic scattering, systematic errors were calculated in bins of ϑ_p. These systematic factors biased the luminosity and, as a result, the global normalization of the breakup cross section. The estimation of systematic errors of differential cross sections for deuteron breakup was performed separately for each configuration defined by ξ or for an individual data point. The global results are presented in Table I, while individual uncertainties of data points are shown as bands in Fig. 13.

The methods adopted to reconstruct physical parameters of the registered particles were investigated as one of the potential sources of systematic errors. Among them, the uncertainties associated with the reconstruction of angles based on the assumption of a point-like target were determined. For that purpose, the reaction point was varied within the volume of the beam-target intersection and a corresponding range of angle variations was determined. The analysis was repeated with all angles shifted within their uncertainty and the resulting change of cross section was included in the systematic uncertainty.

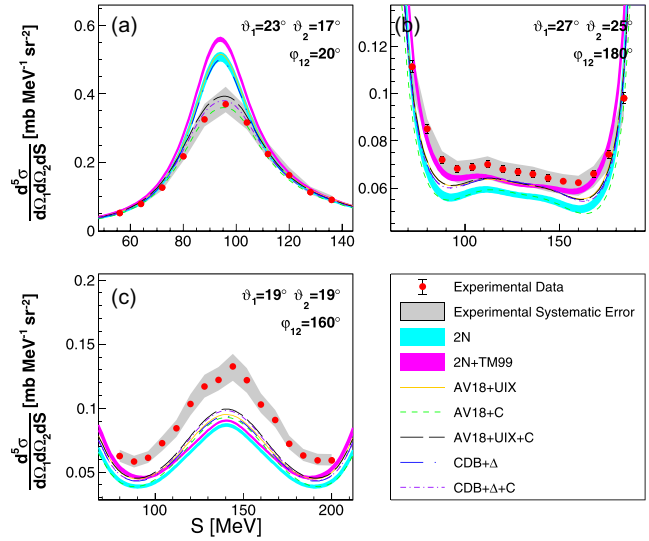

FIG. 13. Examples of cross-section distributions for a few selected configurations specified in the panels. The data are compared with the theoretical predictions for these configurations. Details of theoretical models specified in the legend are included in the paper.

The result of the particle-identification method based on linearization of the ΔE-E spectra was estimated by analyzing the data for different ranges of accepted protons around the corresponding peaks in the $\widetilde{E}$ variable (see Sec. III B). The shape of the PID peaks was not exactly Gaussian, and the corresponding factors were calculated from the real distribution. Ideally, applying these correction factors should result in the same cross-section values for any range of the PID peak used in analysis, with only statistical uncertainties affected. As the PID-related uncertainty, the maximum deviation from this behavior was taken, while the proton acceptance range was varied between 2σ and 3σ of the corresponding peaks. The observed percentage discrepancy for most of the measured cross-section points was below 2% (see Fig. 14), which

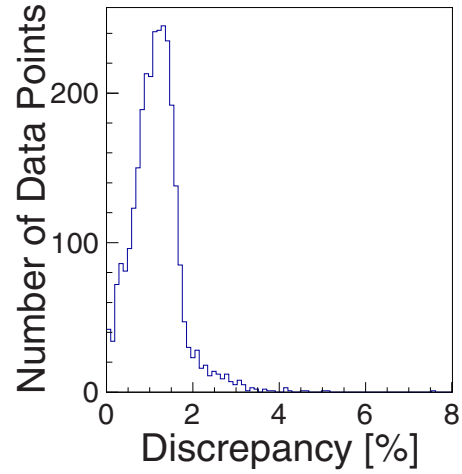

FIG. 14. Distribution of relative difference between the breakup cross-section values obtained with 2σ and 3σ cut on the proton PID peak.

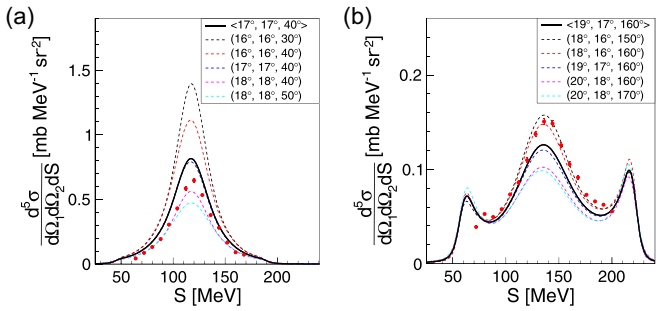

FIG. 15. The effect of averaging (CDB + Δ + C) calculations for a configuration in the region of big variations of the cross sections. Black solid line represents the mean, dashed blue line is the prediction for central geometry, while other dashed lines represent predictions for the limits of accepted angular ranges, each as the function of S along the central kinematic. The experimental data are also presented for comparison (red points).

is adopted as PID-related systematic uncertainty. In the case of elastic scattering, the effect of PID was limited to only one particle, since the coincident deuteron was identified on the basis of strict kinematic relationship of elastic scattering. Here, PID additionally affects the value of luminosity by approximately 0.7%. The systematic uncertainty related to the configurational efficiency had been investigated and presented in detail in a former publication [41]. The discrepancies between different methods of calculations of configurational efficiency presented in that paper allow us to conclude that this uncertainty is low for most of the configurations and it grows with the decrease of relative azimuthal angles, φ_{12}. In particular, the largest contribution corresponds to a few selected configurations characterized by the smallest φ_{12}, while the elastic-scattering channel ($\varphi_{12} = 180^\circ$) is practically untouched by this component.

IV. RESULTS AND DISCUSSION

The measured 2944 points of differential cross sections for 243 geometrical configurations of the deuteron breakup at 160 MeV were used to test modern theoretical calculations.

To account for potential large variations within the theoretical calculations in the finite bin size, the comparison must include cross-section values at the same angular range as in the experiment: $(\vartheta_1 \pm \Delta\vartheta, \vartheta_2 \pm \Delta\vartheta, \varphi_{12} \pm \Delta\varphi)$, where $\Delta\vartheta = 1^\circ$ and $\Delta\varphi = 10^\circ$. The final value representing the theoretical cross section for a given configuration also includes, apart from the central point value, 26 points enclosing the corresponding bin, all of them projected onto a common relativistic kinematics calculated for the central geometry. The S coordinate is defined individually for each configuration, but the same step width, ΔS of 8 MeV, has been set for all. As an example, the data compared with the sample of raw and averaged predictions is presented in Fig. 15. The predicted cross-section values were calculated for (by Witała *et al.*) the set of nucleon-nucleon (2N) phenomenological potentials (CD Bonn [9], Argonne V18 [8], Nijmegen I [10], Nijmegen II [10]) and for these potentials supplemented with the Tucson-Melbourne (TM99) [12] three-nucleon force (2N + TM99).

The next group of calculations (by Deltuva) was based on the Argonne V18 potential in the variants with the added 3N force model of Urbana IX (AV18 + UIX) [11] and taking into account the Coulomb force (AV18 + C, AV18 + UIX + C). Another set of calculations (by Deltuva) is based on the coupled-channel formalism with the charge-dependent Bonn potential with intermediate Δ creation (CDB + Δ) [15], also taking into account the electromagnetic interaction (CDB + Δ + C). Calculations for the 2N phenomenological potentials are presented in the form of bands, the widths of which reflect the range of predictions obtained with individual potentials. The calculations for 2N + TM99 are presented in a similar way, while all other calculations are presented as individual lines. A sample of the measured differential cross section for specific configurations is shown in Fig. 13, demonstrating the crucial role of the Coulomb force [Fig. 13(b)] and the existence of geometries, in which theoretical predictions fail completely [Fig. 13(c)]. For the results for all other configurations, see the additional figures in the Supplemental Material [56]. The data are shown as red dots (full circles) surrounded by the gray bands of systematic errors. Statistical errors are usually smaller than data points. The most striking observation is that the theories overestimate the cross-section values for the configurations with small relative angles φ_{12} and underestimate them for φ_{12} larger than 120°. This effect is visible for all of the investigated polar angle combinations and is consistent with the observations of dp breakup measurement at 130 MeV (65 MeV/nucleon) [23]. The studies performed at 65 MeV/nucleon revealed that the inclusion of the Coulomb interaction practically solved the problem of discrepancy, provided that the 3NF effects were also taken into account. In the present data, the effect is significantly reduced, but not removed for the models including the Coulomb force. In certain areas of phase space the discrepancy between the experiment and the theory is generally significant and cannot be accounted for by the estimated systematical uncertainties. These uncertainties are in most cases comparable or even bigger than the differences between the theoretical predictions based on different calculations with or without the three-nucleon force.

To make a quantitative comparison of the data and the theory and to conclude on the compatibility of the theoretical models with the obtained results, the χ^2 analysis was carried out. The χ^2 variable was calculated for each theoretical model and each geometrical configuration as follows:

$$\chi^2/\text{d.o.f} = \frac{1}{N-1}\sum_{i=1}^{N}\left(\frac{\sigma_i^{\text{expt}} - \sigma_i^{\text{theor}}}{\Delta\sigma_i^{\text{expt}}}\right)^2, \qquad (16)$$

where σ^{expt} corresponds to the measured experimental cross section value, $\Delta\sigma_i^{exp}$ is the total experimental error including both systematic and statistical uncertainties added in squares. σ^{theor} is the prediction of the theory being validated. In case of the 2N and 2N + TM99 calculations, σ^{theor} corresponds to the center of the band. Table II presents global values of χ^2

TABLE II. Calculated global χ^2 including all the presented breakup geometries.

d.o.f.	2944	
2N	4.55	Witała
2N + TM99	3.92	group
AV18 + UIX	3.42	
AV18 + C	3.89	Deltuva
AV18 + UIX + C	2.60	
CDB + Δ	3.51	
CDB + Δ + C	2.74	Deltuva

obtained for all of the presented geometrical configurations. The data presented for a wide spectrum of geometries allowed for selecting the most reliable subset characterized by high experimental statistics, small value of estimated systematic error, and flawless agreement between all of the presented theoretical model predictions. For the dataset selected this way, the agreement between experiment and theory was significantly better [see Figs. 16–18). The calculations based on the 2N interactions alone [see Fig. 16(a)] provided a very good description of the cross-section data in the central part of the examined angular range. The quality of the description deteriorates significantly at low φ_{12} values, where the final-state interactions (FSIs) of the proton pair play a more significant role. In the FSI region, the Coulomb interaction between protons should not be neglected and, indeed, calculations including this ingredient [AV18 + C in Fig. 17(b)] provided results which were much closer to the data in this region. The dominance of the Coulomb interaction in the proton-proton FSI region was also observed in the breakup cross section at other energies [28,57,58]. In extreme cases, such as the $\vartheta_1 = 21^\circ$, $\vartheta_2 = 21^\circ$, $\varphi_{12} = 20^\circ$ configuration (see Fig. 5 in the Supplemental Material [56]), the Coulomb repulsion produces a dip in the middle of the S distribution, at the point corresponding to equal proton energies. Although the addition of the Coulomb force improved description at low φ_{12}, it had no positive influence in other regions of discrepancies and even deteriorated the agreement at $\varphi_{12} \geqslant 140^\circ$ [see Fig. 13(c)]. The remaining discrepancies can be attributed either to the 3NF or relativistic effects. Calculations including 3NF, like AV18 + UIX [Fig. 17(a)], CDB + Δ [Fig. 18(a)], or 2N + TM99 [Fig. 16(b)] showed significant improvement in the whole region of large φ_{12}, but only the calculations including both three-nucleon and the Coulomb forces, AV18 + UIX + C [Fig. 17(c)] and CDB + Δ + C [Fig. 17(b)] provided fairly good descriptions for the majority of the investigated configurations. This success is also reflected in the global values of χ^2 presented in Table II. The significance of 3NF can be agreed upon; on the other hand, the improvement was not always sufficient. Generally, there are two regions of the χ^2 values remaining high. In the first one, at $\varphi_{12} \leqslant 100^\circ$ and the biggest investigated polar angles, $\vartheta_1, \vartheta_2 \geqslant 25^\circ$, all the calculations were higher than the data, and adding 3NF even increased χ^2. In the second one, at $\varphi_{12} \geqslant 140^\circ$, the improvements resulting from the introduction of 3NF were significant, but not sufficient.

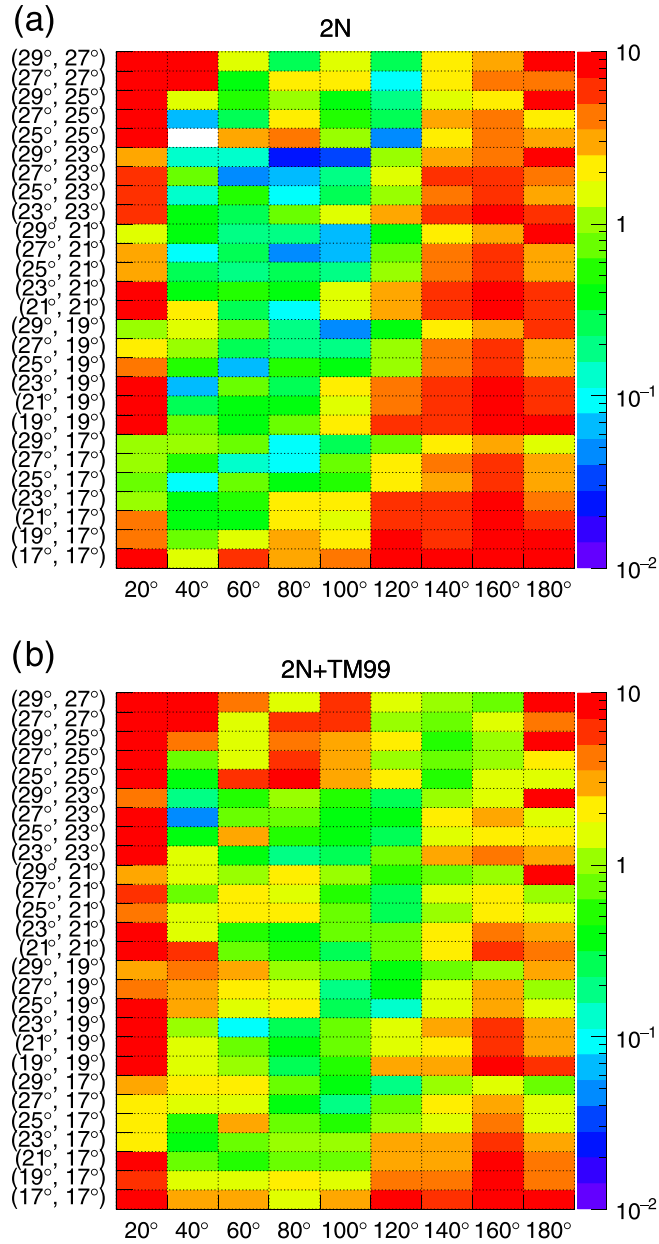

FIG. 16. Maps of χ^2/d.o.f. for individual geometries of the breakup reaction defined by the polar (ϑ_1, ϑ_2 on vertical axis) and azimuthal (φ_{12} on horizontal axis) angles. The data are compared with the center of the bands corresponding to the (a) 2N and (b) 2N + TM99 calculations. For details see the text.

V. SUMMARY

The measurement of ^{1}H(d, pp)n at 80 MeV/nucleon expanded the existing dataset of differential cross sections by 2944 data points for 243 geometrical configurations, creating a dense grid in solid angle limited by $\vartheta \in (17^\circ, 29^\circ)$. A set of models including contributions from two-nucleon interaction combined or not with the 3NF or Coulomb force dynamics was validated with the χ^2-test method, referring each model prediction to cross-section distributions. In conclusion, it was proved that, taking into account the Coulomb

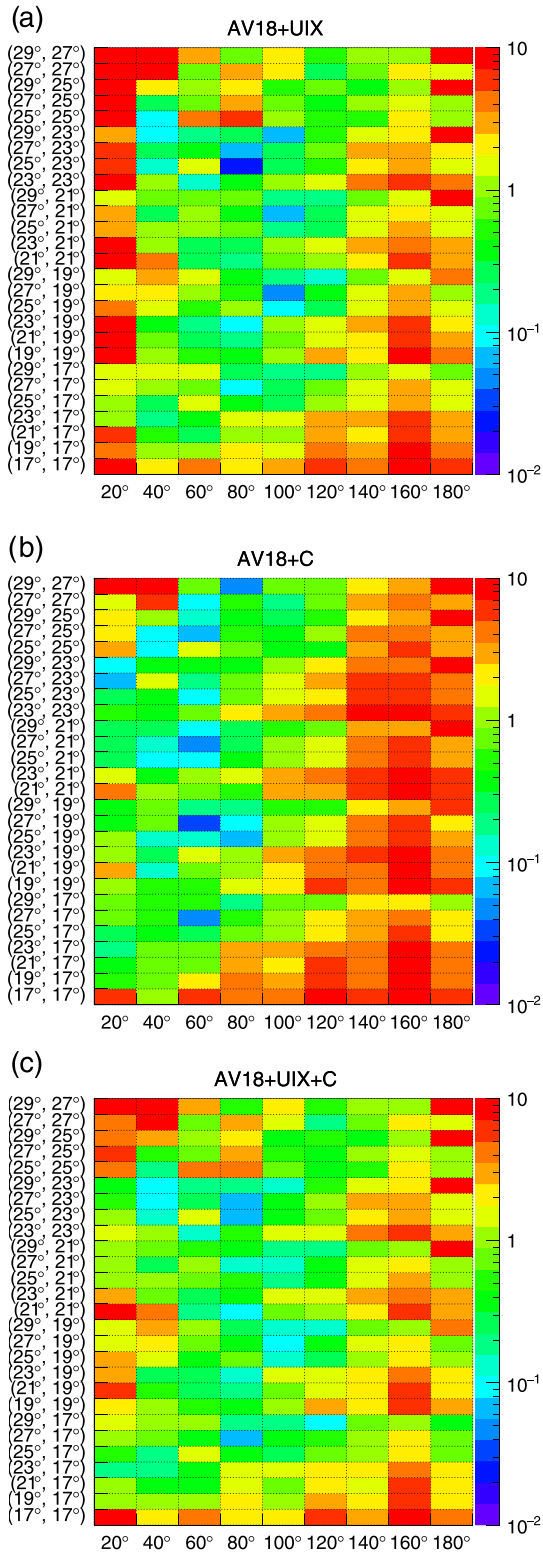

FIG. 17. Similar to Fig. 16 but for the calculations with the AV18 potential in combination with the Coulomb interaction and/or with the Urbana IX force, as specified at the top of each panel.

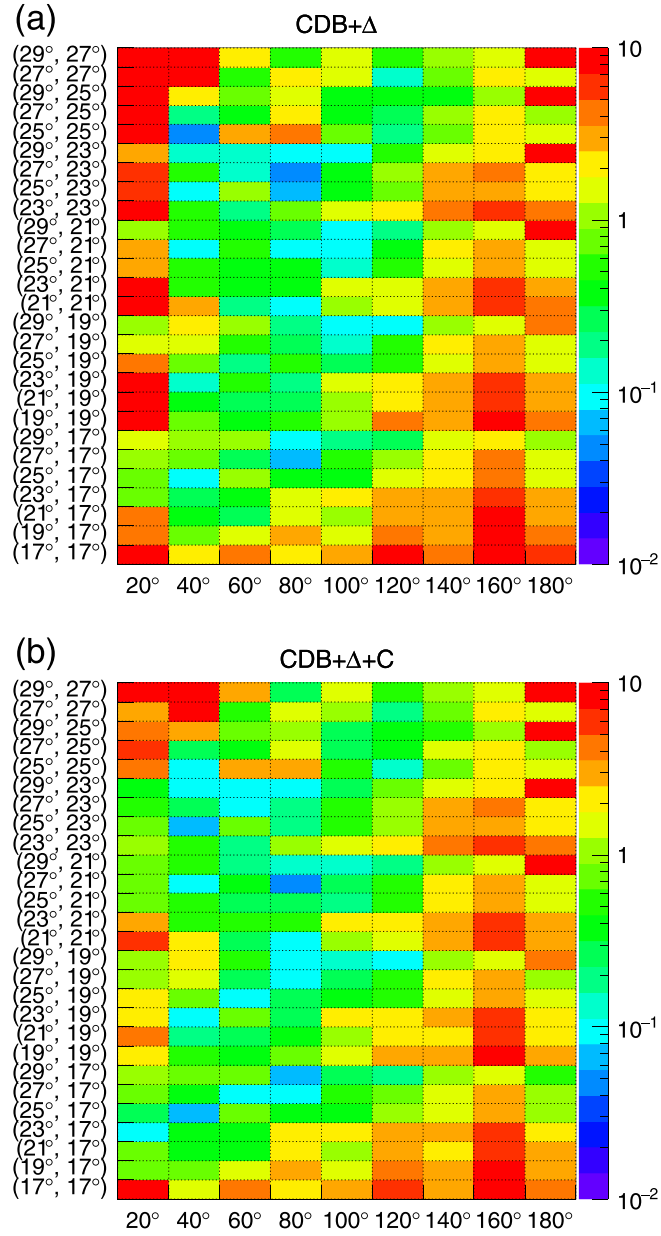

FIG. 18. Similar to Fig. 16 but for the calculations with the CDB + Δ potential, optionally in combination with the Coulomb interaction, as specified at the top of each panel.

and three-nucleon forces for modeling an effective nuclear interaction, globally improves the quality of predictions. The sensitivity of a differential cross section to the Coulomb and 3NF effects varies significantly across the examined phase space. There were also configurations in which none of the models provided satisfactory description of the data. Underestimation of the cross section data by theoretical calculations was also observed in the corresponding phase-space regions of the measurements of the ^{2}H$(p, pp)n$ reaction at 135 and 190 MeV [57,58], and, recently, for the ^{1}H$(d, pp)n$ reaction with 170 MeV/nucleon [59]. This observation clearly shows the difficulty of achieving a correct description of the dynamics of a breakup process, which already appears with relatively low beam energies for cross-section polarization observables. It is worth recalling that a similar difficulty in the description

of differential cross sections of elastic-scattering emerges only above 120 MeV/nucleon [53]. The sources of the discrepancies cannot be clearly identified at present. The solution may be provided by calculations with new potentials developed within ChEFT. The development of fully relativistic calculations with the 3NF and Coulomb force included, as well as a further systematic confirmation of experimental findings, are necessary for the ultimate understanding of the nature of the observed discrepancies.

ACKNOWLEDGMENTS

This work was partially supported by the Polish National Science Center (NCN) from the DEC-2012/05/B/ST2/02556, 2016/22/M/ST2/00173, and 2016/23/D/ST2/01703 grants, and by the European Commission within the Seventh Framework Program through IA-ENSAR (Contract No. RII3-CT-2010-262010). We wish to express our gratitude to the AGOR cyclotron crew and the ion source group for providing us with an excellent and stable beam for the experiment.

[1] F. D. Faddeev, Sov. Phys. JETP **12**, 1014 (1961).
[2] H. Witała, T. Cornelius, and W. Glöckle, Few-Body Syst. **3**, 123 (1988).
[3] D. Hüber, H. Witała, and W. Glöckle, Few-Body Syst. **14**, 171 (1993).
[4] W. Glöckle, H. Witała, D. Hüber, H. Kamada, and J. Golak, Phys. Rep. **274**, 107 (1996).
[5] H. Yukawa, Proc. Phys.-Math Soc. Jpn. **17**, 48 (1935).
[6] G. P. S. Occhialini and C. F. Powell, Nature (London) **159**, 186 (1947).
[7] H. Witała, W. Glöckle, J. Golak, A. Nogga, H. Kamada, R. Skibiński, and J. Kuroś-Żołnierczuk, Phys. Rev. C **63**, 024007 (2001).
[8] R. B. Wiringa, V. G. J. Stoks, and R. Schiavilla, Phys. Rev. C **51**, 38 (1995).
[9] R. Machleidt, Phys. Rev. C **63**, 024001 (2001).
[10] V. G. J. Stoks, R. A. M. Klomp, C. P. F. Terheggen, and J. J. de Swart, Phys. Rev. C **49**, 2950 (1994).
[11] B. S. Pudliner, V. R. Pandharipande, J. Carlson, S. C. Pieper, and R. B. Wiringa, Phys. Rev. C **56**, 1720 (1997).
[12] S. A. Coon and H. K. Han, Few-Body Syst. **30**, 131 (2001).
[13] A. Deltuva, K. Chmielewski, and P. U. Sauer, Phys. Rev. C **67**, 034001 (2003).
[14] A. Deltuva, R. Machleidt, and P. U. Sauer, Phys. Rev. C **68**, 024005 (2003).
[15] A. Deltuva, A. C. Fonseca, and P. U. Sauer, Phys. Lett. B **660**, 471 (2008).
[16] R. Machleidt and D. Entem, Phys. Rep. **503**, 1 (2011).
[17] E. Epelbaum and U.-G. Meißner, Annu. Rev. Nucl. Part. Sci. **62**, 159 (2012).
[18] S. Ishikawa, Few-Body Syst. **32**, 229 (2003).
[19] A. Deltuva, A. C. Fonseca, and P. U. Sauer, Phys. Rev. C **73**, 057001 (2006).
[20] H. Witała, J. Golak, W. Glöckle, and H. Kamada, Phys. Rev. C **71**, 054001 (2005).
[21] R. Skibiński, H. Witała, and J. Golak, Eur. Phys. J. A **30**, 369 (2006).
[22] S. Kistryn and E. Stephan, J. Phys. G Nucl. Part. Phys. **40**, 014006 (2003).
[23] S. Kistryn, E. Stephan, A. Biegun, K. Bodek, A. Deltuva, E. Epelbaum *et al.*, Phys. Rev. C **72**, 044006 (2005).
[24] K. Sekiguchi, H. Sakai, H. Witała, W. Glöckle, J. Golak, K. Hatanaka *et al.*, Phys. Rev. Lett. **95**, 162301 (2005).
[25] M. Eslami-Kalantari *et al.*, Mod. Phys. Lett. A **24**, 839 (2009).
[26] H. Mardanpour *et al.*, Phys. Lett. B **687**, 149 (2010).
[27] S. Kistryn *et al.*, Few-Body Syst. **50**, 235 (2011).
[28] I. Ciepał, B. Kłos *et al.*, Few-Body Syst. **56**, 665 (2015).
[29] R. Machleidt and F. Sammarruca, Phys. Scr. **91**, 083007 (2016).
[30] J. Carlson, S. Gandolfi, F. Pederiva, S. C. Pieper, R. Schiavilla, K. E. Schmidt, and R. B. Wiringa, Rev. Mod. Phys. **87**, 1067 (2015).
[31] G. Hagen, M. Hjorth-Jensen, G. R. Jansen, and T. Papenbrock, Phys. Scr. **91**, 063006 (2016).
[32] E. Epelbaum, J. Golak, K. Hebeler, T. Hüther, H. Kamada, H. Krebs *et al.*, Phys. Rev. C **99**, 024313 (2019).
[33] F. Sammarruca and R. Millerson, Phys. Rev. C **102**, 034313 (2020).
[34] B. Sytze, The Superconducting Cyclotron AGOR: Accelerator for Light and Heavy Ions (1987).
[35] H. Mardanpour and A. Ramazani-Moghadam-Arani, BINA Manual, KVI Groningen (2006), https://www.rug.nl/kvi-cart/research/hnp/bina/binamanual.pdf.
[36] M. Volkerts *et al.*, Nucl. Instrum. Methods Phys. Res., Sect. A **428**, 432 (1999).
[37] *Premium Plastic Scintillators*, Data Sheet (Saint–Gobain SA, 2015) https://www.crystals.saint-gobain.com/document-center/.
[38] E. Stephan *et al.*, Eur. Phys. J. A **49**, 36 (2013).
[39] H. Essel and N. Kurz, IEEE Trans. Nucl. Sci. **47**, 337 (2000).
[40] I. Ciepał *et al.*, Few-Body Syst. **60**, 44 (2019).
[41] I. Ciepał, J. Kuboś, K. Bodek, N. Kalantar-Nayestanaki, G. Khatri, S. Kistryn *et al.*, Phys. Rev. C **99**, 014620 (2019).
[42] M. Kerrisk *et al.*, The Linux Man-Pages Project (2004), http://man7.org/linux/man-pages/man3/atan2.3.html.
[43] J. Płoskonka *et al.*, Nucl. Instrum. Methods **126**, 57 (1975).
[44] W. Parol *et al.*, EPJ Web Conf. **81**, 7019 (2014).
[45] A. Wilczek, Ph.D. thesis, University of Silesia, Katowice, 2010 (unpublished).
[46] W. Parol *et al.*, Acta Phys. Pol., B **45**, 527 (2014).
[47] G. Khatri, Ph.D. thesis, Jagiellonian University, Kraków, 2015 (unpublished).
[48] I. Ciepał, G. Khatri, K. Bodek, A. Deltuva, N. Kalantar-Nayestanaki, S. Kistryn *et al.*, Phys. Rev. C **100**, 024003 (2019).
[49] D. Measday and C. Richard-Serre, Nucl. Instrum. Methods **76**, 45 (1969).
[50] H. Shimizu *et al.*, Nucl. Phys. A **382**, 242 (1982).
[51] M. Davidson, H. Hopkins, L. Lyons, and D. Shaw, Nucl. Phys. **45**, 423 (1963).

[52] K. Sekiguchi, H. Sakai, H. Witała, W. Glöckle, J. Golak, M. Hatano *et al.*, Phys. Rev. C **65**, 034003 (2002).
[53] K. Ermisch, H. R. Amir-Ahmadi, A. M. van den Berg, R. Castelijns, B. Davids, E. Epelbaum *et al.*, Phys. Rev. C **68**, 051001(R) (2003).
[54] H. Witała, W. Glöckle, D. Huber, J. Golak, and H. Kamada, Phys. Rev. Lett. **81**, 1183 (1998).
[55] W. Parol, Ph.D. thesis, Jagiellonian University, Kraków, 2016 (unpublished).
[56] See Supplemental Material at http://link.aps.org/supplemental/10.1103/PhysRevC.102.054002 for full set of measured cross section distributions.
[57] M. Eslami-Kalantari, Ph.D. thesis, University of Groningen, Groningen, 2009 (unpublished).
[58] H. Mardanpuor-Mollalar, Ph.D. thesis, University of Groningen, Groningen, 2008 (unpublished).
[59] P. Adlarson *et al.* (WASA-at-COSY Collaboration), Phys. Rev. C **101**, 044001 (2020).